

III-N/Si₃N₄ Integrated Photonics Platform for Blue Wavelengths

Riazul Arefin¹, Sujit H. Ramachandra, Hyemin Jung, Weicheng You, Syed M. N. Hasan, Henryk Turski, Sarvagya Dwivedi², *Member, IEEE*, and Shamsul Arafin¹, *Senior Member, IEEE*

Abstract—In this paper, we report a low-loss photonic integrated circuits (PICs) platform at blue wavelengths of the visible spectral regime. Silicon nitride (SiN) is a popular passive waveguide material due to its fabrication flexibility, CMOS compatibility and spectral transparency in this wavelength regime. For active devices including lasers, gallium nitride (GaN) and its alloys are considered. Several basic building blocks for the development of a complete integrated platform, including blue diode lasers, in-plane- and out-of-plane light couplers, as well as on-and off-chip coupling between these active and passive components are theoretically investigated. The proposed in-plane and out-of-plane architectures operate through edge- and vertical grating couplers (VGCs), respectively. With edge-coupling, large mode-mismatch between the GaN laser diode and SiN waveguide is alleviated through nanopapers on both the active and passive sections and the calculated peak coupling efficiency is achieved to be 74% at a wavelength of 450 nm. We also separately designed efficient VGCs for coupling light from standard, commercial, off-the-shelf fibers to the SiN chip, and edge couplers for fiber-chip coupling, exhibiting coupling efficiencies of 51% and 83%, respectively. For robust on-chip light-coupling between active and passive circuit elements, with relaxed alignment tolerances, two approaches, i.e., flip-chip based hybrid integration and evanescent coupling based heterogeneous integration are studied. Calculated maximum coupling efficiencies of 40% (−4 dB) are achieved for both the hybrid and heterogeneous schemes. The theoretical work performed is an initial step towards demonstrating complex blue PICs which could offer a comprehensive range of photonic functionalities.

Index Terms—Photonic integrated circuit, silicon nitride, edge-coupler, nanopaper, vertical grating coupler and coupling efficiency.

I. INTRODUCTION

OVER the last 20 years, the field of integrated optics has been revolutionized by silicon photonics [1], [2]. The low-loss, high refractive-index contrast features and CMOS compatibility of the silicon-on-insulator (SOI) technology have

made it a unique medium for the design of high-density photonic integrated circuits (PICs) for conventional telecom- and datacom applications [3]–[5]. Beyond silicon photonics, InP-based monolithic PICs have also witnessed great technological advancements over the past few decades. Such tight photonic integration, however, has not yet reached its full potential in the short-wavelength regime [6]. Given that a complete integrated photonic platform can offer compelling size, weight, power, and cost (SWaP-C) reduction advantages, PICs at visible and near-infrared (NIR) wavelengths are currently receiving significant research interests for a wide range of emerging applications, including biochemical sensing [7], optical interconnects [8], visible light communication [9], bio-imaging, and quantum computing [10]. Developing PICs, especially at blue wavelengths of the visible spectral regime is essential due to magnificent potential in the aforementioned real-world applications.

The SOI system, used in mainstream silicon photonics is not an ideal choice for the development of visible wavelength PICs primarily due to material absorption of silicon at these wavelengths [11]. In addition to spectral transparency, other attractive aspects such as fabrication flexibility, CMOS compatibility and the possibility of obtaining high-quality materials through inexpensive deposition techniques are considered while selecting passive core materials [12]. Based on the above considerations, SiN, TiO₂, and AlN are three potential candidates among materials to be used for the passive platform. AlN, being a high-bandgap material, should theoretically exhibit much less optical absorption at the wavelength of interest [13]. However, depositing high-quality crystalline AlN is challenging due to a large lattice mismatch with sapphire substrates during expensive epitaxial growth [14], making this material less appealing. Although TiO₂ shows some promise [15], high material absorption and lower availability in the conventional deposition systems makes it less popular for the intended applications [16], [17]. An important candidate is the silicon nitride (SiN) waveguide system, in which the silicon core of the SOI-system is replaced by a SiN core while maintaining the CMOS compatibility. The massive potential and research interest for SiN can be justified by the establishment of an open access platform for passive components based on SiN in the visible spectrum [18].

From a point of view of waveguide loss, caused by light scattering and absorption processes, SiN is ideal since the refractive index contrast with SiO₂ is moderately low, which

Manuscript received February 17, 2020; revised April 25, 2020; accepted May 3, 2020. Date of publication May 11, 2020; date of current version May 22, 2020. (Corresponding author: Shamsul Arafin.)

Riazul Arefin, Sujit H. Ramachandra, Hyemin Jung, Weicheng You, Syed M. N. Hasan, and Shamsul Arafin are with the Department of Electrical and Computer Engineering, The Ohio State University, Columbus, OH 43210 USA (e-mail: arafin.1@osu.edu).

Henryk Turski is with the Institute of High Pressure Physics, PAS, 01-142 Warsaw, Poland (e-mail: henryk@unipress.waw.pl).

Sarvagya Dwivedi is with IMEC, 3001 Leuven, Belgium (e-mail: sarvagya.dwivedi@imec.be).

Color versions of one or more of the figures in this article are available online at <http://ieeexplore.ieee.org>.

Digital Object Identifier 10.1109/JQE.2020.2993634

0018-9197 © 2020 IEEE. Personal use is permitted, but republication/redistribution requires IEEE permission.
See <https://www.ieee.org/publications/rights/index.html> for more information.

reduces the waveguide losses arising from sidewall roughness. Given an absorption onset at $\lambda < 420$ nm, SiN can be safely used as a core material in the 450 nm range [13], [19]. This can be evidenced by a recent demonstration of SiN waveguides with loss as low as 2.5 dB/cm [20]. However, the requirement of maintaining single-mode condition in SiN with tight mode confinement at shorter wavelengths leads to an increased vulnerability towards high optical scattering loss, due to waveguide sidewall roughness [20].

Blue lasers as a single component are experimentally demonstrated and commercialized with a reasonably good performance for solid-state lighting and automotive applications [21]. Their monolithic and heterogeneous integrations to develop the PIC technology has also recently been reported by a few research groups [6], [15]. The monolithic approach with GaN-based active and passive components [6] seems less practical from a perspective of integrating high-density photonic circuitry due to processing complexity and high waveguide-loss. Moreover, another recent demonstration on successful heterogeneous integration of III-N blue lasers with TiO₂ waveguides, leveraged the high refractive index of TiO₂, and shows extended research efforts towards developing the PIC technology in the blue wavelengths. Some discrete passive components such as low-loss waveguide and grating couplers on SiN [22], [23], and AlN [13], [14], [24] were also demonstrated in the wavelength range of 532-700 nm. Blue light propagation in the passive SiN photonic platform using an off-chip commercial laser and grating devices was presented in Ref. [25]. However, the demonstration of true on-chip integration is still missing at the blue wavelengths.

In this work, we study the SiN waveguide system with the aim of developing a complete PIC. As basic building blocks, edge- and vertical grating couplers (VGCs) are designed for the blue wavelengths with a peak at 450 nm. Though edge couplers offer high operating bandwidth and efficiency, they require precise post-fabrication processing with a low misalignment tolerance. VGCs, on the other hand, are free from these constraints and have the ability to couple light to and from any part of the circuit, without any post-processing, but, with a compromise on the coupling efficiency (CE) [26]–[28]. This justifies the design of an efficient VGC for robust off-chip light coupling. For the integration of the SiN waveguides and the GaN-light sources, a design based on hybrid integration is also reported, leveraging the VGCs designed in this work and a total internal reflection (TIR)-based mirror. Finally, heterogeneous integration of GaN gain blocks onto SiN through micro-transfer printing is presented. These design details provided in this paper can also be extended for realistic modeling of future SiN PICs at other wavelengths longer than 450 nm.

II. LASER DIODE DESIGN

A standard Fabry–Pérot diode laser based on InGaN/GaN materials is designed for emission at ~ 450 nm. For this design, a shallow-etched ridge waveguide-structure is considered to obtain lateral index-guiding which is important for achieving lasing in the nitride material system. Fig. 1(a) shows the cross-sectional schematic of the laser whose epitaxial structure details can be found in [29]. The narrow ridge width is chosen

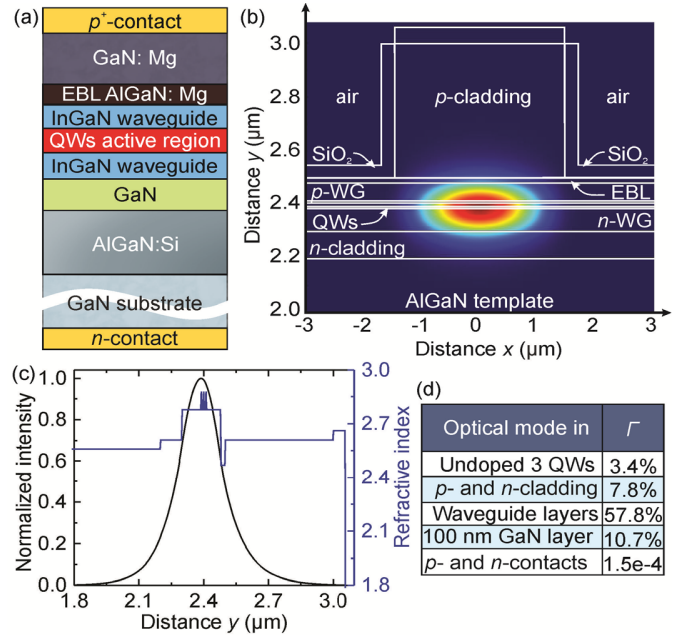


Fig. 1. (a) Epilayer stack of the GaN-based edge-emitting blue lasers, (b) the corresponding 2D fundamental transverse mode, (c) normalized intensity and refractive index profile of the lasers along the growth direction, and (d) confinement factors (Γ) at several important sections of the laser.

to be 3 μm to facilitate single lateral mode emission. For realistic modeling, the ridges are considered with a 250 nm SiO₂ passivation layer on the etched top-surfaces and sidewalls.

Using the complex refractive index profile and appropriate thicknesses of each layer, a 2D optical mode simulation is performed at 450 nm. Fig. 1(b) shows the fundamental transverse electric (TE) mode profile in the device. The intensity distribution, together with the refractive index profile, is also shown in Fig. 1(c). Given that the laser structure employs compressively-strained In_{0.17}Ga_{0.83}N/GaN multiquantum wells (MQWs), the consideration of TE polarized light emission can be justified. For the fundamental TE mode, the effective refractive indices of the device ridge and the etched region (outside the ridge) are calculated to be 2.7 and 2.68, respectively, which results in a numerical aperture (NA) of 0.29.

III. WAVEGUIDE AND OFF-CHIP COUPLING

A. Single Mode Condition

Single-mode propagation is an important requirement for waveguide-based devices to avoid interference from higher-order modes. Considering that, we first investigated the single-mode condition of fully-etched/strip waveguides. Among the most commonly used waveguide structures, the strip waveguide design is considered, owing to strong optical confinement in the core, increased design flexibility and high integration density, due to a small allowable minimum bending radius. A one-dimensional (1D) finite difference Eigen mode (FDE) simulation was first performed to calculate the maximum thickness for the single-mode operation of such SiN strip waveguides, embedded in SiO₂ cladding layers.

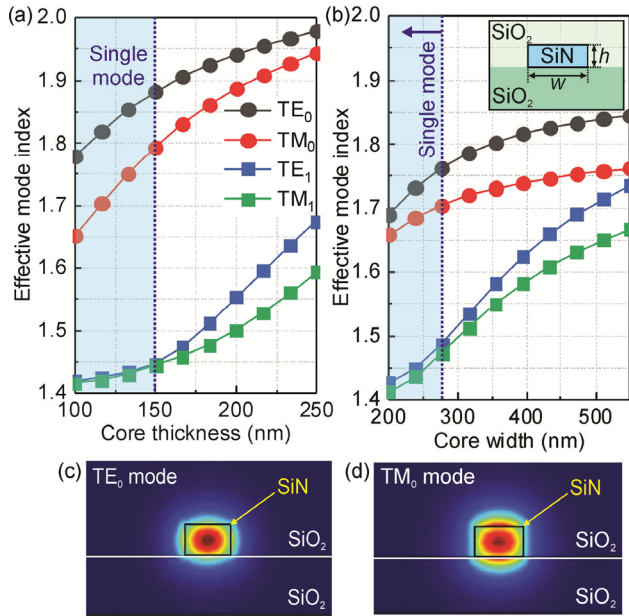


Fig. 2. Effective indices of the fundamental and the first higher order modes of the strip waveguides as a function of core (a) thickness, h and (b) width, w for a fixed core of $h = 125$ nm for both polarizations. The schematic cross-section of the strip waveguides is shown as inset. The cut-off condition of single-mode operation is represented by the vertical dashed line. Fundamental (c) TE and (d) TM mode profiles.

The single-mode waveguide cut-off condition in terms of thickness is around 150 nm, as shown in Fig. 2(a).

A 2D mode simulation was then performed to determine the cut-off width condition for a fixed core thickness of 125 nm. The effective index vs. core width curves of the proposed waveguide structure is shown in Fig. 2(b). For simplicity, the effective indices of only the TE₀, TM₀, TE₁ and TM₁ modes of this waveguide with different widths are shown. The waveguide with a cut-off core width of 270 nm exhibits single-mode operation, allowing both fundamental TE and TM polarizations, as shown in Fig. 2(b). The field profiles of the fundamental TE and TM modes are also presented in Fig. 2(c) and (d), respectively. During the subsequent design of the passive components for wavelengths around 450 nm, the SiN waveguide layer thickness and width values of 125 nm and 220 nm, respectively, were used in order to be well-below the single-mode regime and guide quasi-TE polarized light. The bottom cladding layer with a thickness of $2.4 \mu\text{m}$ prevents the mode leakage into the silicon substrate. The same thickness for the top cladding layer leads to a symmetric optical mode intensity profile, which is important to design an efficient edge-coupler, as discussed in Section III-B. The well documented Palik model [30] for Si-SiO₂, and experimentally-measured refractive index of plasma-enhanced chemical vapor deposition (PECVD) SiN from Ref. [31] were used for all the simulations performed in this study.

B. Edge Coupler Design

Given the immaturity of integration platform at the visible, in particular, blue wavelengths, it is important to design edge-(or butt) coupling structures to connect two different

waveguides in close physical proximity and transfer optical signals between them. Despite being the most straightforward way of coupling light between the two waveguides, inherent optical mode- and effective refractive index mismatches at the waveguide ends make efficient coupling challenging. However, an optimized and careful design of the edge coupler can enhance the CE, characterized by the overlap of the modes in the waveguide ends. The CE between the optical modes at the waveguide ends can be calculated by the overlap integral [32]

$$\eta = \text{Re} \left[\frac{(\int E_1 \times H_2^* \cdot ds)(\int E_2 \times H_1^* \cdot ds)}{\int E_1 \times H_1^* \cdot ds} \frac{1}{\text{Re}(\int E_2 \times H_2^* \cdot ds)} \right]$$

where η is the overlap integral, assuming values between 0 and 1, E_1 and E_2 represent the complex electric field amplitudes of the waveguide mode (at the nanotaper tip) and the fiber mode (at the edge) respectively, and H_1, H_2 represent magnetic fields in the same order. In case of the coupling between GaN laser and SiN waveguide, the same equation holds, with E_2 and H_2 representing the fields within the laser structure.

In this study, the edge-coupling between the optical fibers and SiN chips, termed as “F-C” as well as active lasers and SiN chips termed as “L-C” was investigated. While the L-C couplers transmit light only from a laser diode to the waveguide chip, the F-C couplers couple light at the fiber-waveguide interfaces in a bidirectional fashion. These two different designs were carefully constructed and optimized to achieve a high CE. Unlike standard glass fibers at telecom wavelengths, fewer fiber options are available at this short wavelength. In particular, the commercial-off-the-shelf SM400 fiber [33] was considered while designing the passive waveguides to enable butt-coupling with a reduced mode-mismatch. The mode field diameter (MFD) of an SM400 fiber is about $2.5\text{-}3.4 \mu\text{m}$ [33], which is one order of magnitude higher than the MFD of the SiN waveguides with the single-mode dimensions. In addition, the near-field patterns of the optical modes at these two waveguide ends are not identical. While the SM400 fiber exhibits circularly symmetric mode patterns, the passive SiN waveguide mode has an elliptical shape due to its rectangular cross-section. In comparison to F-C couplers, the L-C end waveguides have similar cross-sections, i.e. rectangular. However, the dimensional difference between the L-C waveguide ends causes the mode mismatch issue in a similar way.

In order to alleviate the inherent problem of the mode mismatch for the couplers, an inverse nanotaper geometry is employed on the SiN waveguides, with the core width progressively narrowed along the length. This leads to a gradual decrease in the mode confinement along the length, and as a consequence, the effective modal area increases and the effective index decreases [34]. In the F-C design, the SM400 fiber [33] was considered to have a mode field diameter between $2.5\text{-}3 \mu\text{m}$ and a NA of 0.13 [33]. Since the core and cladding diameters of the commercial fiber are fixed, the width and length of the horizontal inverse taper are tailored in a way so that the MFD and the effective index of the mode at the output facet of the spot converter can be matched to the fiber for efficient coupling.

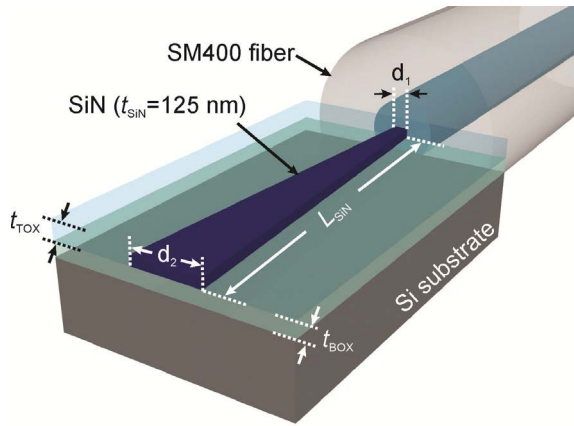


Fig. 3. Schematic of a fiber to chip edge coupler. The SM400 fiber is modeled to properly carry light of 450 nm wavelength.

TABLE I
DIFFERENT PARAMETERS OF TWO EDGE COUPLER DESIGN

Parameter	Fiber to Chip (F-C)	Laser to Chip (L-C)
t_{BOX}	2.4 μm	2.4 μm
t_{TOX}	2.4 μm	2.4 μm
t_{SiN}	125 nm	125 nm
d_1	30 nm	60 nm
d_2	220 nm	220 nm
L_{SiN}	400 μm	400 μm

In the case of the L-C couplers, such an inverse tapering is introduced on both the passive waveguides and the input laser waveguides. In our design, the width of the waveguide at the end of the nanotaper was optimized first to maximize the mode overlap. The taper length was then determined to control the rate of mode expansion and the back-reflection at the input waveguide simultaneously. Fig. 3 shows a schematic of the F-C edge-coupling with all the corresponding relevant design parameters, as listed in Table I. The length of the nanotaper was designed to be 400 μm .

In the L-C coupling, the design challenge is further supplemented by the higher refractive index mismatch between two waveguides defined in the two different material platforms. As compared to SiN with a refractive index of 2.05 in the passive output waveguide, the InGaN/GaN diode laser-based input waveguide has a higher refractive index with 2.8 and 2.4 in the MQWs and cladding layers, respectively. Since the edge coupler is implemented as a nanotaper, the effective index (n_{eff}) of the waveguide mode is seen to be reduced to a value of 1.5 at the tip of the nanotaper, increasing the n_{eff} mismatch. To overcome this problem, we used a waveguide section in the laser structure whose width was gradually tapered down to 60 nm. The value of the reduced width is limited by the resolution of the stepper lithography. Tapering up the SiN passive waveguides in the longitudinal direction to increase the effective index cannot be considered since the overlap integral between the laser and waveguide modes will be reduced due to mode-area mismatch.

Fig. 4 shows the corresponding fundamental TE mode profiles at the input and output waveguide ends for both types of coupling. The effective mode area mismatch between

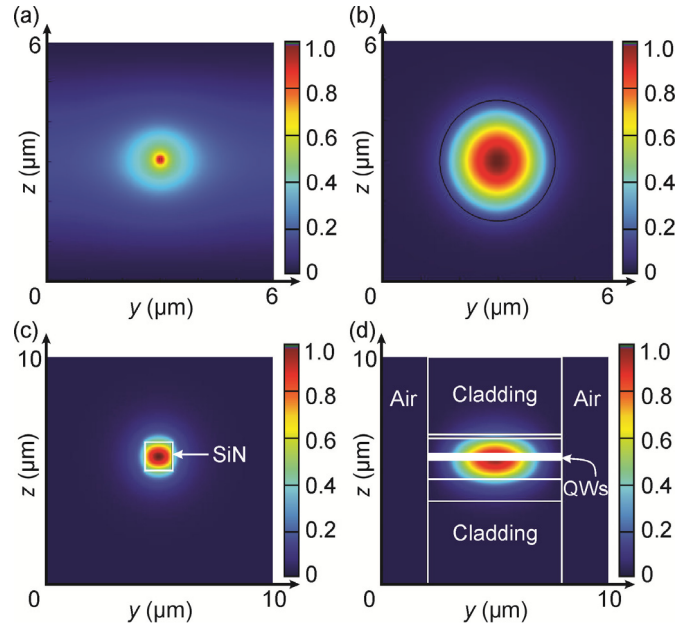


Fig. 4. Mode profile of the (a) nanotaper tip (b) fiber edge for the F-C design and (c) nanotaper tip of the SiN waveguide and (d) tapered laser tip for the L-C design. The mode in the adiabatic SiN tapers in (a) and (c) are designed in such a way so that overlap integral of the modal area of fiber edge and laser tip in (b) and (d) respectively is maximized.

passive SiN waveguides and the optical fibers as well as laser chips, are reduced. Delocalization of the modes at the tips of the SiN and ridge-laser waveguides are also seen here.

To characterize the CE of the two coupler designs, the overlap integrals were calculated. Considering the NA of 0.13 for the commercial fibers, the CE for such an engineered F-C coupler is estimated to be 83% as shown in Fig. 5(a). The maximum CE for the L-C coupler is 74%. Despite the tailored waveguide ends on both designs, the maximum CE is limited by the inherent large mode- and effective refractive index mismatches, owing to a waveguide discontinuity. The insertion losses induced by partial reflections at the interfaces and positional misalignment will further reduce the experimental CE. Both the designs exhibit a reasonably broad spectral response over which the CE remains nearly constant. As shown in Fig. 5(b), the spectral response is nearly flat for a wavelength span of 40 nm for these designs.

The length of the tapers plays a crucial role in gradually expanding the mode and ultimately achieving maximum CE. Fig. 5(c) presents the CE as a function of SiN adiabatic nanotaper length for the F-C couplers. It is seen that the CE converges to the maximum value for a taper length of 400 μm . Introduction of adiabatic tapers on both the laser and passive waveguides of the L-C structures necessitates the taper length optimization on both the active and passive waveguides. The CE vs the taper length of the active waveguide is plotted in Fig. 5(d). At a length of 500 μm , the CE reaches a maximum value of 74%, which is lower than the F-C coupler with the same taper length. This is primarily due to larger effective refractive index mismatch, causing reflections at the SiN/III-N interfaces. Around one-fourth of the incident energy is either reflected back to the source or scattered away,

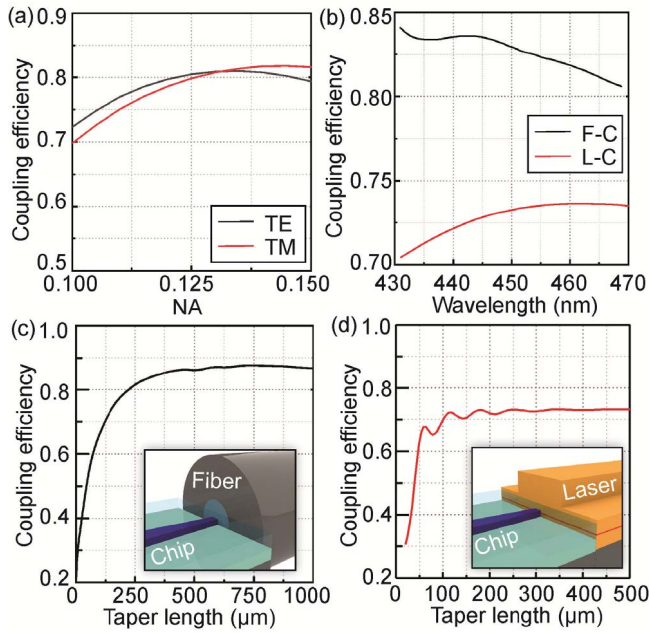


Fig. 5. (a) CE versus NA for the F-C edge coupler. Peak CE of 83% at NA of 0.13 for the fiber. The response is polarization insensitive. (b) CE versus wavelength for two designs, showing a broadband response. (c) CE versus taper length of SiN waveguide for F-C structure. At a taper length of 400 μm , the CE converges to its maximum value. (d) CE versus taper length of ridge laser for L-C design.

resulting in an overall coupling loss due to a difference in the refractive index of the two regions.

In order to assess the performance of the couplers, the dependence of the CE on the positional misalignment is presented in Fig. 6. It is evident that the F-C couplers are more misalignment-tolerant than the L-C ones. This is mainly a consequence of the disparity in the mode profiles of the fiber and the laser. Unlike the circularly-symmetric fiber modes, the laser's elliptical modes require more critical alignment with the passive waveguides. An excess loss of 3-dB is incurred for a misalignment of 1.8 μm and 0.7 μm for the F-C and L-C couplers, respectively. The maintenance of such precise alignment requires careful hermetic post-processing in case of mass production. In addition, standalone device level testing demands a fine piezoelectric control of the chips. Using bulk optics, such as high NA lens in between the coupler and the fiber/laser can solve this issue to some extent. Another interesting approach will be the use of a multi-tip nanotaper [35].

C. Vertical Grating Coupler

Though the edge coupler offers a broadband response and high CE, it provides low misalignment tolerance, requiring compact packaging and post-processing after fabrication. VGCs, on the other hand, can couple light into any part of the circuit without raising the alignment concerns. A typical VGC consists of a first-order grating, whose period can be calculated by the Bragg equation [36]

$$\Lambda = \frac{\lambda}{n_{\text{eff}} - n_c \sin \theta}$$

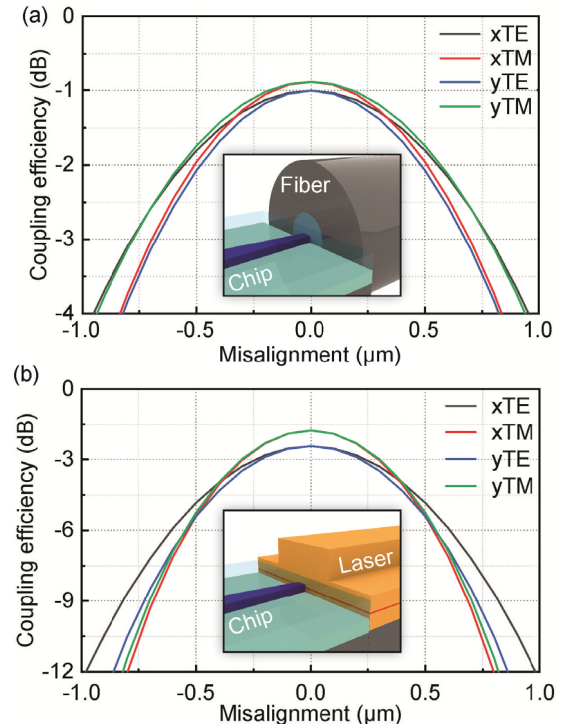


Fig. 6. CE versus positional misalignment for the (a) F-C and (b) L-C designs. Tolerance is comparatively more relaxed for F-C coupler than the L-C one.

where Λ is the grating period, λ the emission wavelength, n_{eff} and n_c the effective indices of the grating and cladding, respectively, and θ is the angle of incidence of light from the fiber to the chip. With the angle of incidence equal to 10° , the period of the grating is optimized to 325 nm at the wavelength of interest.

Unlike the edge-couplers, efficient coupling of light perpendicular to the plane is dependent on satisfying the Bragg's equation which brings a dependency on a number of design parameters including grating period, fill-factor, etch depth, angle of incidence, number of gratings and the buried oxide (BOX) thickness. This requires an iterative process to optimize these parameters with the aim of maximizing the CE. In our design, a well-known particle swarm optimization (PSO) algorithm was utilized to simultaneously optimize these parameters. Using these parameters, a finite-difference time-domain (FDTD) simulation was carried out to verify the results. Fig. 7(a) and (b) show the 3D and 2D views of the vertical grating coupler, respectively.

Among the six design parameters, the BOX thickness plays an important role in improving the CE. The reflections from the BOX – Si substrate interface cause a portion of the light to pass through the gratings for the second time, allowing a greater percentage of the incident energy to be coupled into the waveguide. The thickness of the BOX should ensure that the reflected light reaches the coupler, in-phase with the incident light. Using the PSO algorithm, the period and fill factor of the grating are 325 nm and 48%, respectively. Twelve fully-etched gratings composed of SiN were incorporated in the design. It was seen that a minimum of eight grating teeth are required to ensure diffraction at the VGC and any number

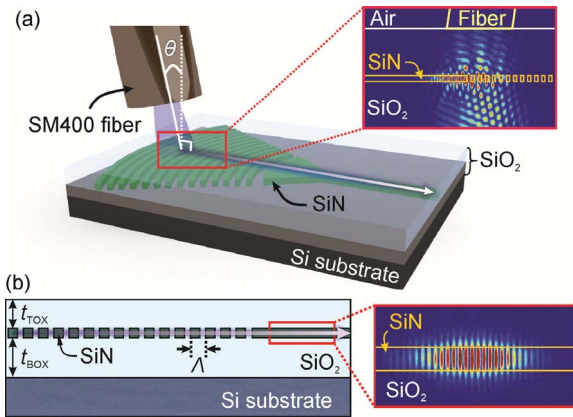


Fig. 7. (a) 3D and (b) 2D cross-sectional structure of the VGC. A fully-etched design is opted for a better CE. The light incident onto the VGC and the resulting mode guided by the SiN waveguide is shown as inset (top-right). A 2D profile of the light guided by the SiN waveguide is shown as inset (bottom-right).

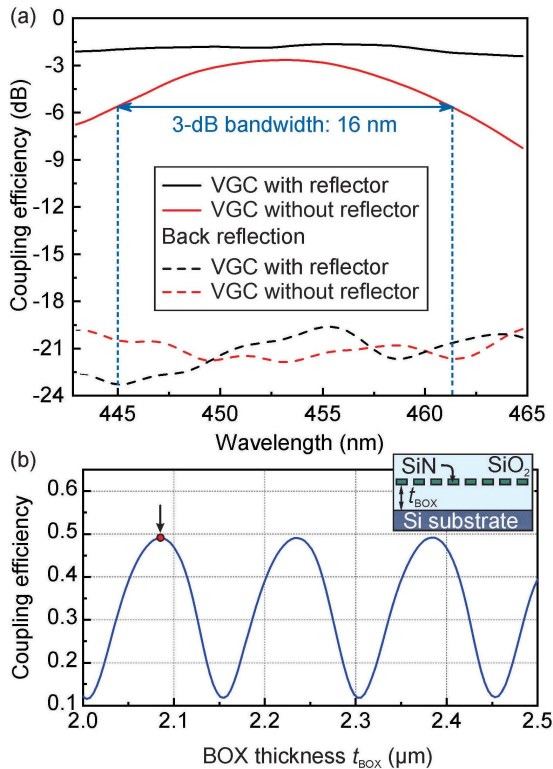


Fig. 8. (a) CE vs wavelength plot for the VGC with and without a metal reflector along with back reflection (b) CE as a function of BOX thickness. A periodic rise and fall of CE with increasing BOX thickness is seen as a result of light being in phase and out of phase with respect to the incident light at the VGC after reflections at the BOX-substrate interface.

upwards of 12 do not affect the CE. The angle of incidence is optimized to a value of 10° .

A simulated peak CE value of -3 dB obtained for the VGC. The back-reflection of the component is as low as 21 dB over the entire wavelength range, as shown in Fig. 8(a), hinting a reasonably good design. Overlays and apodizations were not utilized in the design, thus reducing the complexity from a fabrication standpoint. The simulated 3-dB bandwidth is found

TABLE II
COMPARISON OF REPORTED PERFORMANCE OF EDGE AND VERTICAL GRATING COUPLERS IN THE VISIBLE SPECTRUM

Component	λ (nm)	CE (dB)	Reference
VGC	450	-32.4 to -36.9	[25]
VGC	400	-8.2 (Theoretical), -10 (Experimental)	[38]
VGC	660	-4.2, -2.44 (With metal reflector)	[23]
VGC	532	-6.8	[22]
Edge coupler	638	-3.5 to -5.5, -2.5 (With multi-tip design)	[39]

to be 16 nm. In the above design, the reflections caused by the BOX-substrate interface slightly improve the CE of the VGC. The theoretical curve of CE vs BOX thickness displays peaks at periodic intervals, indicating the reflected light being in-phase with light, incident at the VGC. Consequently, our VGC design uses the smallest allowable BOX thickness which corresponds to the first CE peak of Fig. 8(b), while preventing mode leakage to the substrate.

In order to further improve 3-dB bandwidth and CE by minimizing substrate loss, a metal reflector can be placed in between the substrate and waveguide layers [37]. For our short-wavelength VGCs, the design was modified by inserting a 110-nm-thick CMOS-compatible aluminum (Al) layer at the substrate-BOX interface. As a result, the peak CE is enhanced to -1.7 dB as shown in Fig. 8(a). Though the CE of the VGC is not as high as in the case of the edge coupler, a value of -1.7 dB in the 450 nm wavelength is comparable to other grating couplers reported in visible wavelengths, as listed in Table II. With the metal reflector, the 3-dB bandwidth of the VGCs is improved to 42 nm. The increase in the 3-dB bandwidth is due to the light reflected from the metal layer having a larger power at wavelengths, away from the peak of the VGCs transfer function.

IV. HYBRID INTEGRATION OF BLUE LASERS AND SiN PICs

Integration strategies including heterogeneous integration and flip-chip bonding based hybrid integration at 1550 nm are adopted for conventional telecom and datacom applications. A hybrid integration technique reported in [40] is incorporated in our design as it facilitates efficient coupling and provides an added advantage of heat sinking via the top contacts due to flip-chip configuration. This method has been proven to be thermally stable and has the potential to improve performance through more sophisticated structures, compatible for laser integration. This reflective semiconductor optical amplifier (RSOA) based hybrid, integrated waveguide bonded to a silicon substrate is shown in Fig. 9(a). In this technique, a total internal reflection (TIR) mirror is used at the end of the integrated waveguide nanotaper, to redirect light onto a VGC for coupling into the PIC. Effective hybrid integration using a surface ridge laser is mainly reliant on mode dilution in the III-V laser into a relatively thick bottom

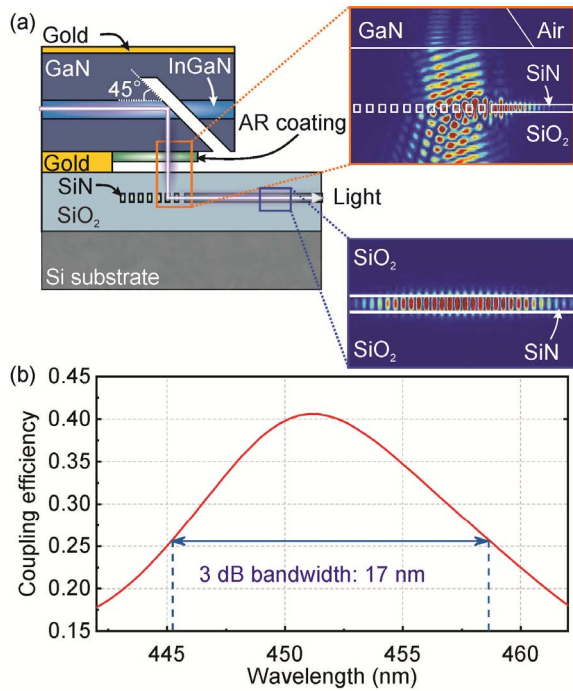


Fig. 9. (a) Schematic of the flip-chip hybrid integration approach (b) CE as a function of wavelength.

waveguide layer. In addition, since the flip-chip configuration is used, the surface ridge lies in the path of the light reflected from the TIR mirror and can distort the mode, reducing the CE. The work in [41] addresses these concerns by using a nanotaper for mode dilution and a spot size converter to overcome mode distortion at the ridge.

Fig. 9(a) shows a 2D cross-section of the design for hybrid integration at the end of the nanotaper. The structure consists of an In_{0.17}GaN waveguide layer of 1.4 μm thickness, serving as the core and a GaN cladding layer to guide light of 450 nm wavelength. A 45° angle cut is used to place the TIR mirror to direct light into the VGC positioned below, which maximizes the CE. Such angular cuts can be realized in the III-V region, either by using chemically-assisted ion beam etching (CABIE) [40] or the focused ion beam etching (FIB) [42] method. To minimize reflections at the multiple interfaces, an AR coating is used at the aperture, located at the base of the laser. A gold layer is incorporated for bonding as it enhances the thermal stability of the whole integrated structure and facilitates lasing operation.

Based on the described geometry, 2D FDTD simulations were run to maximize the coupling between the lasers and the SiN waveguides. The light incident on the VGC, and the corresponding mode, coupled into the SiN waveguide, is shown in the inset of Fig. 9(a). A 3-dB bandwidth of 17 nm is obtained from the optimized design, which yields a maximum CE value of 40% at 450 nm, as presented in Fig. 9(b). A major factor which conspires to reduce the CE of the design is the mode mismatch between the optical field from the laser, which reduces the coupling. Methods to improve the CE include an addition of DBR mirrors and metal layers below the VGC at a specific distance, to reflect the

light back into the VGC for another pass, which theoretically increases the CE. However, such methods present additional challenges during the fabrication process and involve a larger number of interfaces which could contribute to higher losses. Potential techniques to improve the CE involve more sophisticated designs of the VGC, involving apodizations and overlays which break the symmetry of the VGC, minimizing the energy lost to the substrate. A partial-etch grating coupler can lead to improved coupling, as the structure is inherently asymmetric.

V. HETEROGENEOUS INTEGRATION OF BLUE LASERS AND SiN PICs

Comparable to hybrid integration, a heterogeneous integration technique offers a reliable way of integrating active and passive components [43]. However, due to a large effective refractive index mismatch between the III-N and SiN waveguides, mode transfer to the SiN passive section becomes challenging. A simple design with engineered waveguide structures on both active and passive sections, for successful heterogeneous integration, is shown in Fig. 10(a). Transfer printing is one of the novel integration strategies that can be adopted for transferring III-N gain blocks onto the SiN platforms [44]. The GaN laser is tapered in two steps, the first consists of the *n*-doped cladding and *n*-waveguide with a longer taper length, and the latter consisting of the MQW active region as well as the *p*-doped region. The thickness of each layer is consistent with that shown in section II of laser diode design, except for a thinner *n*-cladding. To match the mode in the GaN section, tapers were introduced in the SiN waveguide as well. A rib waveguide design is used in the SiN platform where the rib height and etch depth were 250 nm and 125 nm, respectively.

Using an Eigenmode expansion (EME) solver, simulations were run in the tapered structure to confirm the mode transfer into the passive section. In Fig. 10 (b), (c) and (d) the fundamental TE mode profiles from points along the taper are presented. In Fig. 10(b), the mode is predominantly confined in the high-index, active region of the GaN laser. Nanotapers in the GaN section subsequently helps transfer the mode towards the passive SiN section. In Fig. 10(c) the mode profile is shown at the nanotaper tip. As can be seen, the mode begins to transition from III-N to SiN. Finally, Fig. 10(d) shows the mode in the SiN waveguide, beyond the end of the nanotaper.

The EME simulation was run to optimize the taper for adiabatic mode transfer, and a maximum coupling loss of 4 dB was achieved maintaining back reflections as low as -22 dB. Although tapers introduced in the laser cavity may give rise to unpumped regions, and consequently increase the threshold current density, the tapers are essential to transfer the mode to the SiN waveguide. Simulating the same structure with a straight SiN waveguide section leads to a decline in the coupling to 7.9 dB, indicating a clear trade-off with efficient coupling. Such a preliminary design will help towards achieving a highly-efficient mode transfer platform which can be realized by performance-tailored

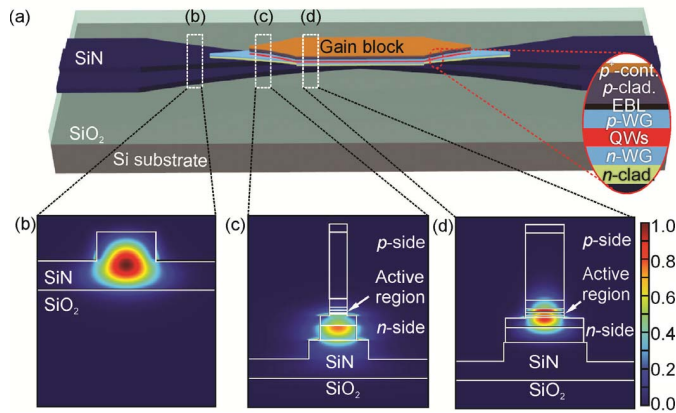


Fig. 10. (a) Schematic of the multi-step tapered heterogeneous integration platform, with tapers in both the GaN and the SiN sections (b) Mode profile of the fundamental TE mode at the nanotaper tip of the p -region, a thickness of 60 nm in the n -side and 30 nm in the p - and MQW region helps to transfer the mode towards the SiN waveguide section. (c) XZ monitor of mode transformation from the laser to the SiN waveguide and (d) from SiN waveguide to GaN laser.

structures, including subwavelength gratings, two-dimensional tapering etc.

VI. CONCLUSION

In summary, a few important active and passive photonic components are designed and simulated. These components are essential building blocks that can enable a whole new class of devices or subsystems with a variety of optical functions in this spectral regime. In particular, this study initially reports a design of blue lasers and their compatibility and integrability with passive SiN circuits. Among basic optical passive components, edge- and VGCs are carefully designed to get a peak performance at a wavelength of 450 nm. Our optimal design allows achieving CEs of 83% and 51% for the edge-couplers and VGCs, with fiber, respectively. Hence, a reasonably good theoretical performance of these passive elements can be claimed by comparing the CE values of similar components at higher wavelengths. Through the hybrid technique, on-chip integration utilizing the VGCs and TIR-mirrors is also presented, and a CE of 40% is achieved. Further engineering on the designs of each component is possible to improve their performances. This, however, will introduce more complexities and challenges in terms of device fabrication and integration. The light's diffraction limit and the associated shortcomings of the traditional fabrication process impose a great challenge on obtaining the desired feature sizes of these components operating at the very-short wavelengths. Finally, this theoretical work is expected to lay a realistic foundation for fabrication and testing of these components to prove the feasibility of the integration work at blue wavelengths. This study will eventually pave the way towards developing emerging architectures that can enable breakthrough capabilities for strategic positioning, navigation, and timing (PNT), sensing, quantum information and visible light communications.

REFERENCES

- [1] B. Jalali and S. Fathpour, "Silicon photonics," *J. Lightw. Technol.*, vol. 24, no. 12, pp. 4600–4615, Dec. 2006.
- [2] D. Thomson *et al.*, "Roadmap on silicon photonics," *J. Opt.*, vol. 18, no. 7, Jun. 2016, Art. no. 073003.
- [3] L. Vivien *et al.*, "Light injection in SOI microwaveguides using high-efficiency grating couplers," *J. Lightw. Technol.*, vol. 24, no. 10, pp. 3810–3815, Oct. 2006.
- [4] D. Taillaert, P. Bienstman, and R. Baets, "Compact efficient broadband grating coupler for silicon-on-insulator waveguides," *Opt. Lett.*, vol. 29, no. 23, pp. 2749–2751, Dec. 2004.
- [5] G. Roelkens, D. Van Thourhout, and R. Baets, "High efficiency silicon-on-insulator grating coupler based on a poly-silicon overlay," *Opt. Express*, vol. 14, no. 24, pp. 11622–11630, Nov. 2006.
- [6] F. Tabataba-Vakili *et al.*, "Demonstration of critical coupling in an active III-nitride microdisk photonic circuit on silicon," *Sci. Rep.*, vol. 9, no. 1, Dec. 2019, Art. no. 18095.
- [7] L. R. Polstein and C. A. Gersbach, "Light-inducible spatiotemporal control of gene activation by customizable zinc finger transcription factors," *J. Amer. Chem. Soc.*, vol. 134, no. 40, pp. 16480–16483, Oct. 2012.
- [8] M. D. Brubaker *et al.*, "On-chip optical interconnects made with gallium nitride nanowires," *Nano Lett.*, vol. 13, no. 2, pp. 374–377, Feb. 2013.
- [9] E. Xie *et al.*, "High-speed visible light communication based on a III-nitride series-biased micro-LED array," *J. Lightw. Technol.*, vol. 37, no. 4, pp. 1180–1186, Feb. 15, 2019.
- [10] S. T. Jagsch *et al.*, "A quantum optical study of thresholdless lasing features in high- β nitride nanobeam cavities," *Nature Commun.*, vol. 9, no. 1, Dec. 2018, Art. no. 564.
- [11] R. Baets *et al.*, "Silicon photonics: Silicon nitride versus silicon-on-insulator," in *Proc. Opt. Fiber Commun. Conf.*, Anaheim, CA, USA, 2016, pp. 1–3, Paper Th3J.1.
- [12] R. Soref, "Mid-infrared photonics in silicon and germanium," *Nature Photon.*, vol. 4, no. 8, pp. 495–497, Aug. 2010.
- [13] G. N. West *et al.*, "Low-loss integrated photonics for the blue and ultraviolet regime," *APL Photon.*, vol. 4, no. 2, Feb. 2019, Art. no. 026101.
- [14] M. Soltani, R. Soref, T. Palacios, and D. Englund, "AlGaIn/AlN integrated photonics platform for the ultraviolet and visible spectral range," *Opt. Express*, vol. 24, no. 22, pp. 25415–25423, Oct. 2016.
- [15] T. Kamei, T. Kamikawa, M. Araki, S. P. DenBaars, S. Nakamura, and J. E. Bowers, "Research toward a heterogeneously integrated InGaIn laser on silicon," *Phys. Status Solidi A*, vol. 217, no. 7, Apr. 2020, Art. no. 1900770.
- [16] J. Wang *et al.*, "Influence of nitrogen doping on device operation for TiO₂-based solid-state dye-sensitized solar cells: Photo-physics from materials to devices," *Nanomaterials*, vol. 6, no. 3, p. 35, 2016.
- [17] C. O. Ayieko, R. J. Musembi, S. M. Waita, B. O. Aduda, and P. K. Jain, "Structural and optical characterization of nitrogen-doped TiO₂ thin films deposited by spray pyrolysis on fluorine doped tin oxide (FTO) coated glass slides," *Int. J. Energy Eng.*, vol. 2, no. 3, pp. 67–72, May 2012.
- [18] IMEC-BioPIX150. SiN-Photonics BioPIX. Accessed: Apr. 23, 2020. [Online]. Available: <https://europractice-ic.com/mpw-prototyping/siphotonics/imec/>
- [19] C. Sorace-Agaskar *et al.*, "Multi-layer integrated photonics from the ultraviolet to the infrared," *Proc. SPIE*, vol. 10510, Feb. 2018, Art. no. 105100D.
- [20] W. D. Sacher *et al.*, "Visible-light silicon nitride waveguide devices and implantable neurophotonics probes on thinned 200 mm silicon wafers," *Opt. Express*, vol. 27, no. 26, pp. 37400–37418, Dec. 2019.
- [21] S. Nakamura *et al.*, "InGaIn-based multi-quantum-well-structure laser diodes," *Jpn. J. Appl. Phys.*, vol. 35, no. 1B, pp. L74–L76, Jan. 1996.
- [22] J. H. Song *et al.*, "Grating devices on a silicon nitride technology platform for visible light applications," *OSA Continuum*, vol. 2, no. 4, p. 1155, Apr. 2019.
- [23] S. Romero-García, F. Merget, F. Zhong, H. Finkelstein, and J. Witzens, "Silicon nitride CMOS-compatible platform for integrated photonics applications at visible wavelengths," *Opt. Express*, vol. 21, no. 12, pp. 14036–14046, Jun. 2013.
- [24] T.-J. Lu *et al.*, "Aluminum nitride integrated photonics platform for the ultraviolet to visible spectrum," *Opt. Express*, vol. 26, no. 9, pp. 11147–11160, Apr. 2018.
- [25] L. Hoffman *et al.*, "Low loss CMOS-compatible PECVD silicon nitride waveguides and grating couplers for blue light optogenetic applications," *IEEE Photon. J.*, vol. 8, no. 5, pp. 1–11, Oct. 2016.
- [26] L. Chrostowski and M. Hochberg, *Silicon Photonics Design: From Devices to Systems*. Cambridge, U.K.: Cambridge Univ. Press, 2015.

- [27] R. Marchetti, C. Lacava, L. Carroll, K. Gradkowski, and P. Minzioni, "Coupling strategies for silicon photonics integrated chips," *Photon. Res.*, vol. 7, no. 2, pp. 201–239, Jan. 2019.
- [28] S. Dwivedi *et al.*, "Multicore fiber link with SiN integrated fan-out and InP photodiode array," *IEEE Photon. Technol. Lett.*, vol. 30, no. 22, pp. 1921–1924, Nov. 15, 2018.
- [29] C. Skierbiszewski *et al.*, "True-blue laser diodes with tunnel junctions grown monolithically by plasma-assisted molecular beam epitaxy," *Appl. Phys. Express*, vol. 11, no. 3, Mar. 2018, Art. no. 034103.
- [30] E. D. Palik, *Handbook of Optical Constants of Solids*. London, U.K.: Academic, 1998.
- [31] A. Gorin, A. Jaouad, E. Grondin, V. Aimez, and P. Charette, "Fabrication of silicon nitride waveguides for visible-light using PECVD: A study of the effect of plasma frequency on optical properties," *Opt. Express*, vol. 16, no. 18, pp. 13509–13516, Sep. 2008.
- [32] A. W. Snyder and J. D. Love, *Optical Waveguide Theory*. London, U.K.: Chapman & Hall, 1983.
- [33] *Thorlabs, SM400 Fiber*. Accessed: Feb. 13, 2020. [Online]. Available: <https://www.thorlabs.com/thorproduct.cfm?partnumber=SM400>
- [34] M. Papes *et al.*, "Fiber-chip edge coupler with large mode size for silicon photonic wire waveguides," *Opt. Express*, vol. 24, no. 5, pp. 5026–5038, Mar. 2016.
- [35] Y.-C. Tu, P.-H. Fu, and D.-W. Huang, "High-efficiency ultra-broadband multi-tip edge couplers for integration of distributed feedback laser with silicon-on-insulator waveguide," *IEEE Photon. J.*, vol. 11, no. 4, pp. 1–13, Aug. 2019.
- [36] W. H. Bragg and W. L. Bragg, "The reflection of X-rays by crystals," *Proc. Roy. Soc. London A, Containing Papers Math. Phys. Character*, vol. 88, no. 605, pp. 428–438, Jul. 1913.
- [37] W. S. Zaoui *et al.*, "High-efficient CMOS-compatible grating couplers with backside metal mirror," in *Proc. 38th Eur. Conf. Exhib. Opt. Commun.*, Amsterdam, The Netherlands, Sep. 2012, pp. 1–3.
- [38] Y. Sohn, Y. Park, D. Suh, H. Ryu, and M. C. Paek, "Focusing grating coupler for blue laser light," *IEEE Photon. Technol. Lett.*, vol. 16, no. 1, pp. 162–164, Jan. 2004.
- [39] J. R. Ong *et al.*, "Silicon nitride double-tip fiber-to-waveguide edge couplers at visible wavelengths," in *Proc. Conf. Lasers Electro-Opt./Pacific Rim*, Singapore, Jul./Aug. 2017, pp. 1–3, Paper s1840.
- [40] B. Song, C. Stagaescu, S. Ristic, A. Behfar, and J. Klamkin, "3D integrated hybrid silicon laser," *Opt. Express*, vol. 24, no. 10, pp. 10435–10444, May 2016.
- [41] B. Song, "3D hybrid integration for silicon photonics," Ph.D. dissertation, Dept. Elect. Eng., Univ. California, Santa Barbara, Santa Barbara, CA, USA, 2019.
- [42] B. Song, S. Pinna, Y. Liu, L. Megalini, and J. Klamkin, "3D hybrid integrated lasers for silicon photonics," *Proc. SPIE*, vol. 10537, Feb. 2018, Art. no. 105370V.
- [43] A. W. Fang, H. Park, O. Cohen, R. Jones, M. J. Paniccia, and J. E. Bowers, "Electrically pumped hybrid AlGaInAs-silicon evanescent laser," *Opt. Express*, vol. 14, no. 20, pp. 9203–9210, Oct. 2006.
- [44] B. Corbett, R. Loi, W. Zhou, D. Liu, and Z. Ma, "Transfer print techniques for heterogeneous integration of photonic components," *Prog. Quantum Electron.*, vol. 52, pp. 1–17, Mar. 2017.

Riazul Arefin received the B.S. degree from the Islamic University of Technology, Gazipur, Bangladesh, and the M.S. degree from École Normale Supérieure Paris-Saclay, Cachan, France. He is currently pursuing the Ph.D. degree with the Electrical and Computer Engineering Department, The Ohio State University. His research interests include silicon photonics, nanophotonics, optoelectronics, etc.

Sujit H. Ramachandra received the B.E. degree from the R. V. College of Engineering, Bengaluru, India. He is currently pursuing the M.S. degree in electrical and computer engineering with The Ohio State University, as a part of the OPREL Lab. His research interests include silicon photonics, and lasers and integrated optics.

Hyemin Jung was born in Daegu, South Korea. She is currently a member of the Optics and Photonics Research Laboratory, Electrical and Computer Engineering Department, The Ohio State University. Her research interests include nanofabrication, photonics sensors, photonic integrated circuits, high power semiconductor laser, and optoelectronics.

Weicheng You was born in Sichuan, China. He received the B.S. degree in electronics engineering from Sichuan University, Sichuan, China, in 2017, and the M.S. degree in electrical engineering from The Ohio State University, Columbus, OH, USA, in 2019, where he is currently pursuing the Ph.D. degree.

Syed M. N. Hasan was born in Dhaka, Bangladesh. He received the B.S. degree in materials and metallurgical engineering from the Bangladesh University of Engineering and Technology, Dhaka, Bangladesh, in 2012, and the M.S. degree in materials science and engineering from the Gwangju Institute of Science and Technology, Gwangju, South Korea, in 2015. He is currently a Graduate Student in Ph.D. Program with the Electrical and Computer Engineering Department, The Ohio State University.



Henryk Turski is currently working as a Senior Researcher with the Institute of High Pressure Physics Unipress Polish Academy of Sciences. He is an Expert in growth of nitride structures by plasma-assisted molecular beam epitaxy. For the last ten years, he was developing epitaxy of optoelectronic devices with main interest in blue-green laser diode structures.



Sarvagya Dwivedi (Member, IEEE) received the master's degree in electrical engineering from the Indian Institute of Technology, Bombay, and the Ph.D. degree in photonics engineering from Photonics Research Group, Ghent University–imec, Belgium. He then worked as a Postdoc Research Associate at the University of California Santa Barbara, Santa Barbara, CA, USA. Prior to joining his Ph.D., he worked as an Applications Engineer and later as a Manager at COMSOL Multiphysics, where he was responsible for providing device and system-level solutions in the area of RF, MEMS and heat transfer. He is currently working as a Senior Photonic Researcher with IMEC, Belgium, where he is developing beam forming networks for LiDAR and imaging applications. He has authored and coauthored over 30 publications in the areas of all-silicon, silicon nitride and Ge-on-Si based tolerant devices and circuits for various applications, such as datacom, telecom, and mid-infrared sensing. He is a member of the OSA, and IEEE Photonics Society. He is an Active Reviewer of the IEEE PHOTONICS TECHNOLOGY LETTERS, the IEEE JOURNAL OF LIGHTWAVE TECHNOLOGY, the IEEE JOURNAL OF SELECTED TOPICS IN QUANTUM ELECTRONICS, OSA *Optics Express*, and *Optics Letters*, respectively. He has served as a Program Committee Member and the Session Chair for the various IEEE and OSA conferences.



Shamsul Arafin (Senior Member, IEEE) is currently working as an Assistant Professor with the Electrical and Computer Engineering Department, The Ohio State University. He has 12 years of experiences on the design, fabrication of widely tunable semiconductor lasers, including vertical-cavity surface emitting lasers (VCSELs). Till now, he has authored or coauthored over 100 publications in the areas of III-V materials, the corresponding devices and InP-based photonic integrated circuits, and has given numerous invited and contributed talks at various international conferences. He has chaired, served on technical committees for IPR in OSA Advanced Photonics, and IEEE Photonics Conference. Over the last decade or so, his research interests center around III-V compound semiconductor nanotechnology for materials and devices: molecular beam epitaxial growth and characterization of thin films (and nanoscale) materials as well as realization of novel optoelectronic devices. His current research interests include design and characterization of GaN and GaSb-based photonic devices for a wide range of emerging applications. He is a Senior Member of the OSA and SPIE.